UNIVERSITYOF BIRMINGHAM

University of Birmingham Research at Birmingham

Active screen plasma surface co-alloying of 316 austenitic stainless steel with both nitrogen and niobium for the application of bipolar plates in proton exchange membrane fuel cells

Lin, Kaijie; Li, Xiaoying; Tian, Linhai; Dong, Hanshan

Link to publication on Research at Birmingham portal

Available online at www.sciencedirect.com

ScienceDirect

journal homepage: www.elsevier.com/locate/he
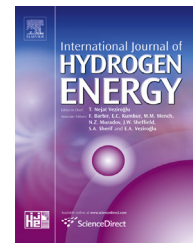
Active screen plasma surface co-alloying of 316 austenitic stainless steel with both nitrogen and niobium for the application of bipolar plates in proton exchange membrane fuel cells

CrossMark

Kaijie Lin[*], Xiaoying Li, Linhai Tian, Hanshan Dong

School of Metallurgy and Materials, The University of Birmingham, Birmingham B15 2TT, UK

ARTICLE INFO

ABSTRACT

Austenitic stainless steel has been researched as a promising candidate material for bipolar plates in proton exchange membrane fuel cells. However, its interfacial contact resistance (ICR) is about 16 times higher that of the Department of Energy (DOE) target (10 mΩ cm^2), which leads to undesirable fuel cell performance. In this work, a new hybrid plasma surface engineering process, based on active screen plasma co-alloying, has been developed to simultaneously alloy 316 austenitic stainless steel (316 SS) surfaces with both nitrogen and niobium. The results demonstrated that the layer structure of the modified surfaces can be tailored by adjusting the treatment conditions. All the plasma treated 316 SS samples exhibited significantly reduced ICR below the DOE target of 10 mΩ cm^2. The corrosion resistance of the N/Nb co-alloyed 316 SS was much better than active screen plasma nitrided and marginally better than the untreated material.

Introduction

As an efficient, clean and quite power source, proton exchange membrane fuel cells (PEMFCs) have received extensive interest in the last decade mainly due to the concerns over severe air pollution caused by conventional power sources and the depletion of fossil energies. Significant improvement has been made recently in the efficiency and performance of PEMFCs. However, the wide commercial application of PEMFCs has been retarded, to a large extent, by the low mechanical strength and the high fabrication cost of graphite bipolar plates [1].

To this end, great efforts have been made to explore metallic bipolar plates, such as aluminium alloys [2,3], titanium alloys [4,5] and amorphous alloys [6,7]. Among them, austenitic stainless steels (SS) have attracted more and more attention as promising candidates for bipolar plate application mainly because of their good mechanical performance, relatively low cost and ease of manufacture

[8−10]. However, there are still some limitations of austenitic stainless steels and hence technical challenges to be addressed. For example, their insufficient corrosion resistance [11,12] and poor conductivity due to the formation of passive oxide layer [13,14] can lead to undesired degradation of the power output of PEMFCs. It is known that surface modification has been successfully used to improve the surface properties of materials and components. Hence, it could be a promising method to improve the surface conductivity and/or corrosion resistance of stainless steel bipolar plates [15−18].

In our recent paper, a low-temperature active screen plasma nitriding (ASPN) technique is reported to modify the surface properties of 316 SS [19]. The surface conductivity of 316 SS has been successfully improved by the low-temperature ASPN induced nitrogen-supersaturated S-phase case. For example, the interfacial contact resistance (ICR) can be reduced from 158 mΩ cm^2 for the as-received 316 SS to 33 mΩ cm^2 for the ASPN treated surfaces. However, the ICR of the ASPN treated 316 SS surface is still larger than the target (10 mΩ cm^2) set by Department of Energy (DOE) [20]. Clearly, alloying with interstitial nitrogen along cannot meet the DOE target and new plasma surface co-alloying techniques with both interstitial and substitutional alloying elements could be a desirable approach.

Niobium and its compounds are well-known for their excellent corrosion resistance and surface conductivity. Many researchers have applied niobium coating onto the surface of stainless steel bipolar plates to improve their performance in PEMFC environment. Different methods have been explored such as cladding [21,22], physical vapour deposition (PVD) [23,24] and electro-deposition [25] to improve the corrosion resistance and surface conductivity of stainless steel. However, the bonding strength between Nb layer and the substrate is low after annealing treatment [26]. Electro-deposition of Nb improves the corrosion resistance of 304 SS but leads to the degradation of surface conductivity due to the formation of NbO and Nb$_2$O$_5$.

In view of the problems associated with Nb coatings, Feng et al. [27] utilizes ion implantation method to introduce Nb into 316 SS. The corrosion current density of the Nb implanted 316 SS is reduced effectively but due to the formation of Nb oxide, the surface conductivity of the Nb implanted stainless steel is still much higher than the DOE target of 10 mΩ cm^2.

Clearly, new surface engineering technologies need to be developed to further improve the surface electrical conductivity of 316 SS. This paper reports a new hybrid plasma surface technology which combines low-temperature active screen plasma co-alloying with both nitrogen and niobium with deposition of a thin surface niobium layer on the top. The microstructure and composition of the plasma treated surfaces were fully studied by X-ray diffraction (XRD), energy dispersive spectroscopy (EDS), X-ray photoelectron spectroscopy (XPS) and scanning electron microscopy (SEM). The surface conductivity and corrosion behaviour were also evaluated. Experimental results have demonstrated that the ICR of the plasma co-alloyed 316 SS surfaces is well below the DOE target (10 mΩ cm^2).

Materials and methods

Materials and sample preparation: Commercial 316 austenitic stainless steel (316 SS) was selected as the substrate, and its chemical composition is (wt%): 0.06% C, 17.20% Cr, 1.30% Mn, 2.20% Mo, 11.70% Ni, 0.014% S and Fe balanced. Coupon samples of 6 mm in thickness were cut off from 1 inch (25.4 mm) hot rolled bars using a SiC cutting wheel. The front side of the coupon samples was firstly wet ground using silicon carbide abrasive paper up to #1200 grit and subsequently polished using 6 μm and 1 μm diamond pastes. The backside was wet ground up to #1200 grit. Prior to treatment, samples were washed with soapy water, cleaned with acetone in ultrasonic bath for 5 min, and finally dried under hot flowing air.

Cross sections were cut from treated coupon samples and mounted in conductive bakelite. The mounted samples were wet ground and then polished using the same procedures as described above. In order to reveal the micro-structure of the cross sections, an etching agent containing 25 ml H$_2$O, 25 ml HNO$_3$ and 50 ml HCl was used. After etching for about 20 s, samples were rinsed immediately with water then acetone, and dried in hot flowing air.

Active screen plasma treatments: Active screen plasma surface co-alloying treatments with both N and Nb (ASPA(N + Nb)) were conducted in an AS Plasma Metal 75 kVA industrial scale furnace and the experimental setting for the ASPA(N + Nb) treatment is shown in Fig. 1, schematically.

The small metal active screen was placed on the worktable of the large furnace, where bias was applied. The lid of the active screen was specially designed to carry niobium. The sample was insulated by ceramic and hence stayed at a floating potential. The effect of bias on the small metal active screen was studied using three different biases: 5%, 10% and 15% of the main power supply of 15 kVA, and the treatment parameters as well as the sample codes are listed in Table 1.

Characterization methods: The phase constituent of the plasma treated samples was investigated using XRD (Bruker D8 Advance) with Cu Kα radiation (λ = 0.154 nm). The surface morphology and the cross-sectional microstructure of the samples before and after treatment were observed using SEM (Jeol 7000). The chemical compositions of the treated surfaces and cross-sections were examined by EDS (Oxford Instrument Inca). The composition and chemical state of the elements were analysed by XPS (Theta Probe). Elemental concentration depth profiles were determined by glow discharge optical emission spectroscopy (GDOES) (Leco GDS-750). The hardness depth profiles were probed using nano-indentation (Nano Test 600).

Corrosion tests: The corrosion behaviour of untreated and plasma treated 316 SS samples under different conditions was evaluated by electrochemical tests consisting of potentiodynamic polarization and potentiostatic polarization. A standard three electrodes system was employed in the polarization tests. A platinum rod, a saturated calomel electrode (SCE) and the to-be-measured sample were acted as the counter electrode, the reference electrode and the working electrode, respectively. The Gamry electrochemical workstation was used to measure and record the corrosion data. To simulate the working environment of PEMFC, a sulphuric acid
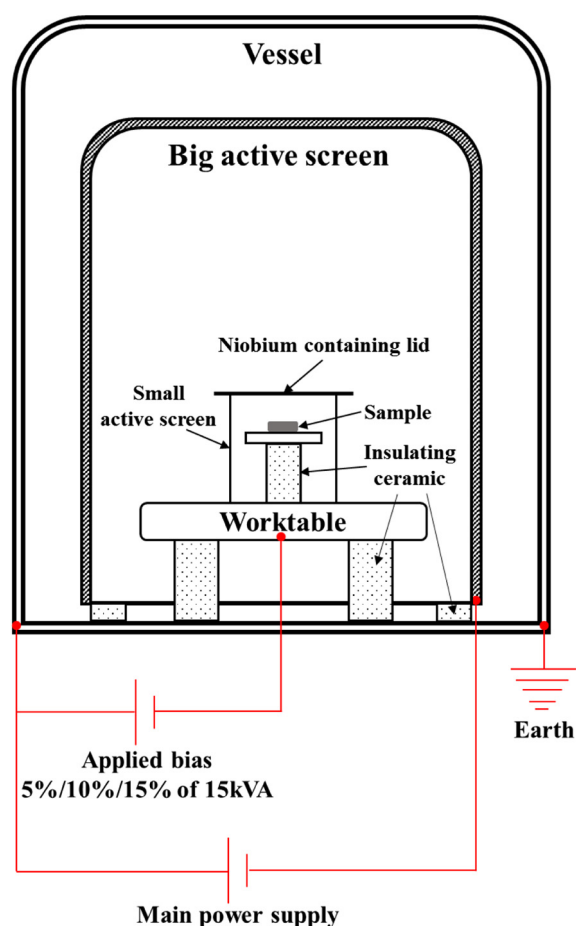
Fig. 1 — Schematic diagram of experimental setting.

aqueous solution (0.5 M H_2SO_4 + 2 ppm HF) was selected as the corrosion solution. Prior to the potentiodynamic polarization, an open circle potential (OCP) test was conducted for 1 h to stabilize the sample in the corrosion solution. The potentio-dynamic polarization scan started from −0.6 V (vs SCE) to 1.2 V (vs SCE) at a sweep rate of 1 mV/s. For the potentiostatic po-larization, constant potentials of 0.6 V (vs SCE) and −0.1 V (vs SCE) were applied to the sample for 4 h, to simulate the cathode and anode environment, respectively.

Interfacial contact resistance: The interfacial contact resis-tance was measured using Wang's method [28]. In brief, the to-be-measured sample was sandwiched between two pieces of carbon paper (Tory 120), and further sandwiched between two copper plates under a compaction force of 140 N/cm². A constant current was applied onto this assembly cell through the copper plates. By measuring the voltage drop of this cell, the total resistance can be calculated. A micro-ohm meter (TTi BS407) was used to apply the current and present the resis-tance directly. To eliminate the influence of the back side of

the sample, gold-coating was applied on it, so the resistance could be neglected.

Results

Surface morphology of ASPA(N + Nb) samples

The surface morphology and composition of the active-screen plasma N/Nb co-alloyed i.e. ASPA(N + Nb) treated samples as a function of the applied bias (Bs) are shown in Fig. 2. It can be seen that the surface morphology was similar for the 5%Bs sample (Fig. 2(a)) and 10%Bs sample (Fig. 2(b)), which consisted of particles with a similar size of about 100 nm. However, when increased the applied bias to 15% (Fig. 2(c)), the size of surface particles became uneven with very small particles and relatively larger clusters but the density of the surface layer was improved with reduced number of pinholes. The EDS surface composition of the three ASPA(N + Nb) treated sam-ples is compared in Fig. 2(d). It can be seen that the content of the alloyed Nb increased markedly with the increase of the bias used; in contrast, the content of Cr, Ni and Fe decreased with the increase of the bias used. The light element N was measured using XPS and the results are re-ported in Section 3.2.2.

Phase constitute of the ASPA(N + Nb) treated surfaces

XRD
The XRD patterns of ASPA(N + Nb) treated samples under different applied biases are plotted in Fig. 3. It can be seen from the XRD profile of the 5%Bs sample that an additional set of peaks can be observed apart from the peaks of the austenitic stainless steel substrate. Comparing with the peaks of the substrate, those additional peaks moved to a lower angle and were broaden to some extent. These are charac-teristic features of the S-phase formed in low-temperature plasma nitrided austenitic stainless steel [29]. However, comparing with the XRD data in the literature [19], the angle shifting of the 5%Bs sample is relatively smaller, which will be discussed in Section 4.2. No peaks of niobium nitride could be found from the XRD pattern of the 5%Bs sample. For the samples treated by 10% and 15% bias, apart from the peaks of the substrate, the peaks of Nb_4N_5 can also be detected. The dominated orientation of Nb_4N_5 changed from (211) for the 10%Bs sample to (310) for the 15%Bs sample. No peaks of S-phase can be found from the XRD patterns of the 10%Bs and 15%Bs samples.

XPS
The chemical states of Nb, N and Fe in ASPA(N + Nb) treated surfaces were analysed by XPS and the spectrums were

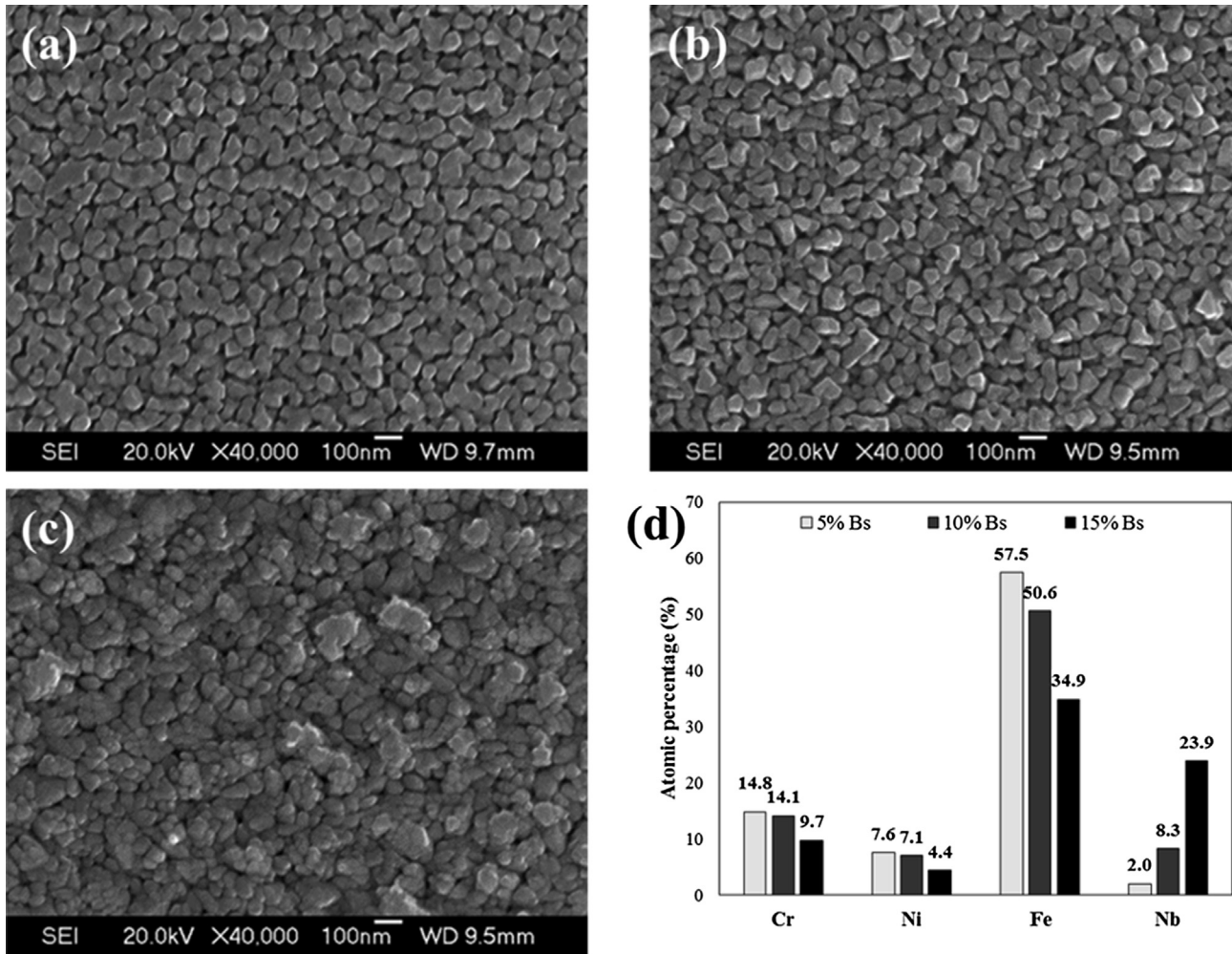| Table 1 — Plasma treatment parameters and sample codes.					
Sample	Temperature (°C)	Duration (h)	Gas	Pressure (mbar)	Applied bias (% of 15 kVA)
5% Bs	450	10	25%N_2 + 75%H_2	0.75	5
10% Bs					10
15% Bs					15

Fig. 2 − Surface morphology of the ASPA(N + Nb) treated samples at different biases: (a) 5% Bs, (b) 10% Bs and (c) 15% Bs together with (d) the EDS surface composition.

obtained after argon ions sputtering for 60s, 180s, 360s and 540s. The XPS spectrums of N 1s and Nb 3d for 5%Bs sample are shown in Fig. 4(a) and (b). It can be seen from these XPS spectrums that the binding energy of N 1s and Nb 3d did not
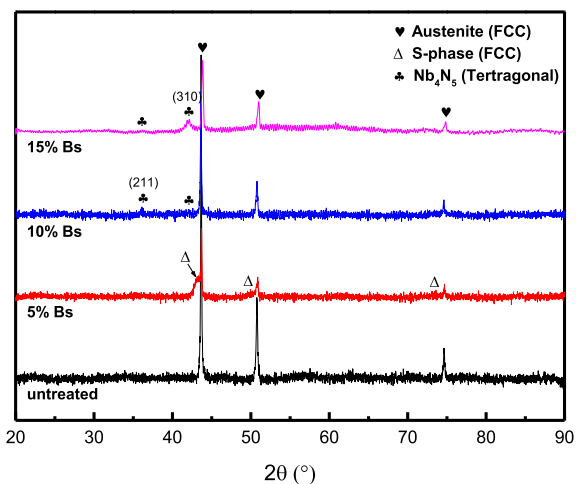
Fig. 3 − XRD profiles of ASPA(N + Nb) samples.

change significantly with the sputtering time (or depth). The binding energy of N 1s was determined to be 397 eV, which was lower than that of the standard binding energy of N 1s (398.4 eV). The binding energy of Nb 3d was identified as 203.4 eV and 206.3 eV, which were higher than the corresponding standard binding energy of metallic niobium (202.3 eV and 205 eV). The obtained values of the binding energy of Nb 3d and N 1s were in good agreement with the results reported by other researchers [30] and the deviation from the standard binding energy implied the formation of niobium nitride. Other conclusions can also be drawn from Fig. 4(a) and (b) are that the intensity of the Nb 3d and N 1s spectrums decreased with the increase of the sputtering time, and the peak of Nb 3d totally vanished but N 1s still remained after sputtering for 540s. Taking the relatively low sputtering rate of XPS into account, the niobium nitride layer formed on the 5% Bs sample must be very thin. Such a thin niobium nitride layer was difficult to be detected by XRD, resulting in the absence of niobium nitride peaks in the XRD pattern of the 5%Bs sample (Fig. 3).

The N and Nb spectrums of 10%Bs and 15%Bs samples are shown in Fig. 4(c) and (d) and (e) and (f), respectively. It can be

Fig. 4 — The N1s and Nb3d XPS spectrums of ASPA(N + Nb) samples: (a)&(b) 5%Bs, (c)&(d) 10%Bs, (e)&(f) 15%Bs and (g) the quantitative XPS results at 360s sputtered surfaces.
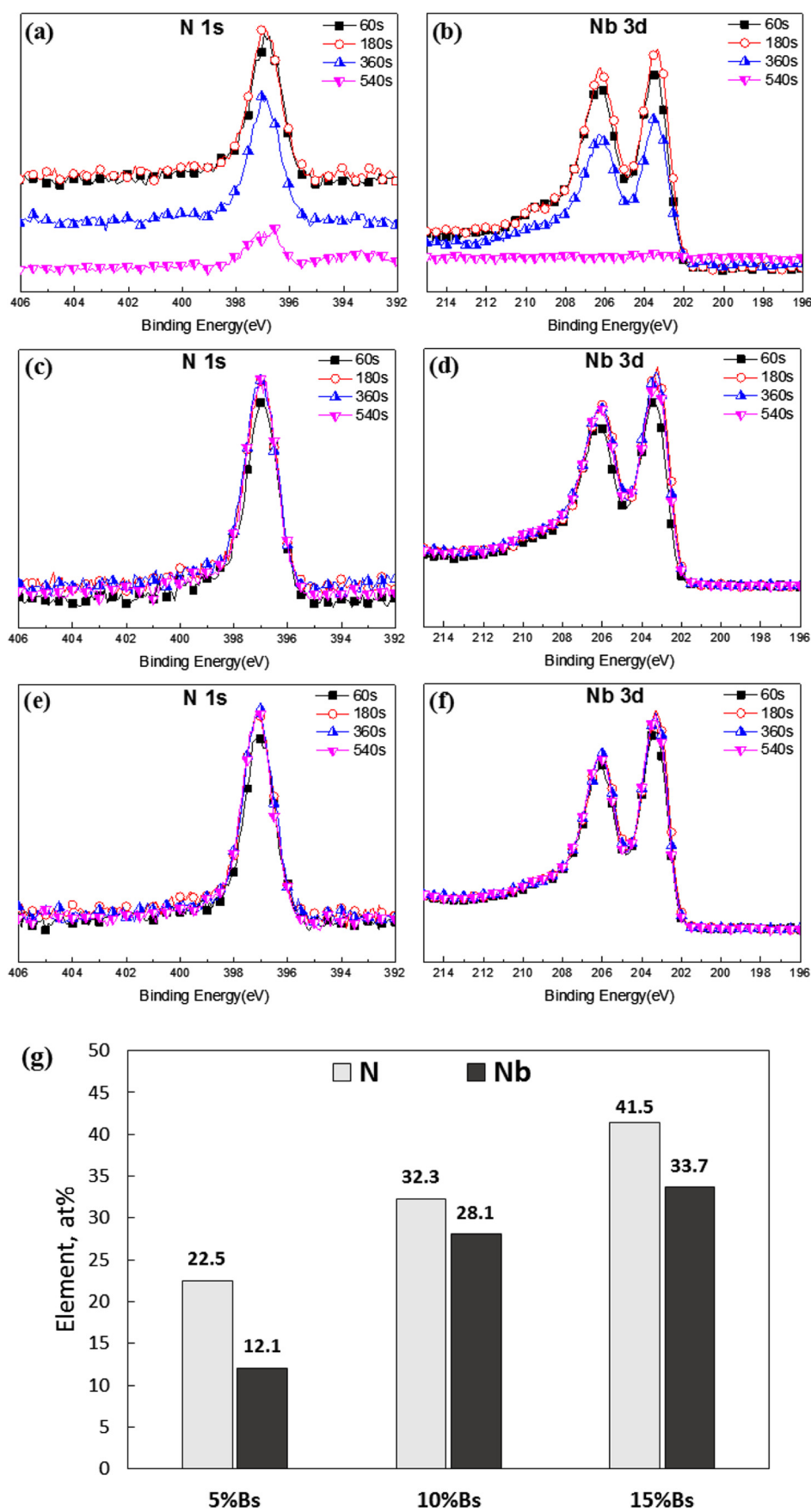
seen that the N and Nb spectrums obtained from the 10%Bs sample were the same as those from the 15%Bs sample. Except for the spectrums of 60s-sputtered surface, other spectrums of 180s, 360s and 540s sputtered surfaces exhibited almost identical profiles. The binding energy of N 1s and Nb 3d identified from the surfaces of the 10%Bs and the 15%Bs samples was the same as that determined from the 5%Bs sample. Therefore, the XPS results of the 10%Bs and the 15%Bs samples also indicated the formation of a niobium nitride layer on the surface of these two samples and the niobium nitride layers were thicker than that formed on the surface of the 5%Bs sample as these spectrums were independent of the sputtering time up to 540s.

The spectrums obtained after argon irons sputtering for 360s were quantitatively analysed and the results are summarized in Fig. 4(g). It can be cleanly seen that the atomic percentage of N and Nb increased with the increase of the applied bias. The identification of Nb_4N_5 peaks from the XRD patterns (Fig. 3) was in agreement with the quantification analysis of the XPS spectrums. The atomic ratio of N/Nb for the 15%Bs sample was around 1.23, which was close to that of the Nb_4N_5 (1.25).

Apart from niobium and nitrogen, iron was also detected by XPS. The binding energy of iron was determined to be 706.7 eV and the peak position did not change after different sputtering durations (Fig. 5). It follows that iron existed in pure metal state in the modified surfaces, and the intensity of the Fe 2p peaks reduced gradually with the increase of applied bias. The content of Fe quantified from the XPS spectrums of 360s sputtered surfaces decreased with the increase of the applied bias from 30.5 at% for the 5% Bs samples to 17.0 at% for the 10% Bs samples and 8.2 at% for the 15% Bs samples. A very low amount of chromium and nickel was found by XPS as well and identified in pure metal state. Most probably, they were sputtered from the stainless steel cage and then deposited on the plasma treated surfaces.

Layer structure of the ASPA(N + Nb) treated samples

The low and high magnification cross-sectional images of ASPA(N + Nb) treated samples are shown in Fig. 6. The samples observed under low magnification were etched, while the samples observed under high magnification were not etched to optimally reveal the microstructural features.

For the sample treated with 5% bias (i.e. 5%Bs), a featureless layer was found on the top of the surface in the low

magnification SEM image (Fig. 6(a)). The GDOES nitrogen depth profile as inlet in Fig. 6(a) indicated the high nitrogen content in this featureless layer. The maximum nitrogen content was found to be around 15 at% in this featureless layer, which was much higher than that of the maximum solid solubility of N in austenitic stainless steel (8.7 at%), reported in literatures [31,32]. Referring to the typical features observed in the previous research [19] and taking the XRD results (Fig. 3) into account, this layer can be identified as the nitrogen supersaturated expanded austenite, i.e. the so-call S-phase [29]. Under high magnification, a dark thin layer was observed on the top of the S-phase case formed on 5%Bs sample (Fig. 6(b)). The EDS element line-scan indicated that this thin dark layer was rich in niobium.

For 10%Bs and 15%Bs samples, a white dense layer can be found on the top of the severely eroded substrate and no S-phase case can be found from those two samples (Fig. 6(c) and (e)). In addition, a groove can be observed between the white layer and the substrate. From the high magnification back-scattered electron (BSE) images of the 10% Bs and 15% Bs samples (Fig. 6(d) and (f)), it can be seen that the top layer was dense and columnar structured, which was in agreement with the surface morphology observed under SEM (Fig. 2). The EDS line-scan also proved that the surface layer contained a high level of niobium. Taking the results of SEM, XPS and XRD into account, the niobium rich layer on the surface could be deduced as the Nb_4N_5 layer. The formation of the groove observed after etching (Fig. 6(c) and (e)) was most probably due to the huge difference in corrosion resistance between the top Nb nitride layer and the substrate. The thickness of the niobium nitride layer and the S-phase case is compared in Fig. 6(g) as a function of the bias used. It can be seen that the thickness of the niobium nitride layer increased with the increase of the applied bias.

Corrosion behaviour

The potentiodynamic polarization curves of ASPA(N + Nb) treated samples are drawn in Fig. 7(a). It can be seen clearly that the ASPA(N + Nb) treated samples exhibited more positive corrosion potential than that of the untreated and typical ASPN treated samples. The passive current density of the ASPA(N + Nb) treated samples was higher than that of the untreated sample but lower than that of the typical ASPN treated sample. It is also noted that in general the passive current density reduced with the increase of the applied bias.
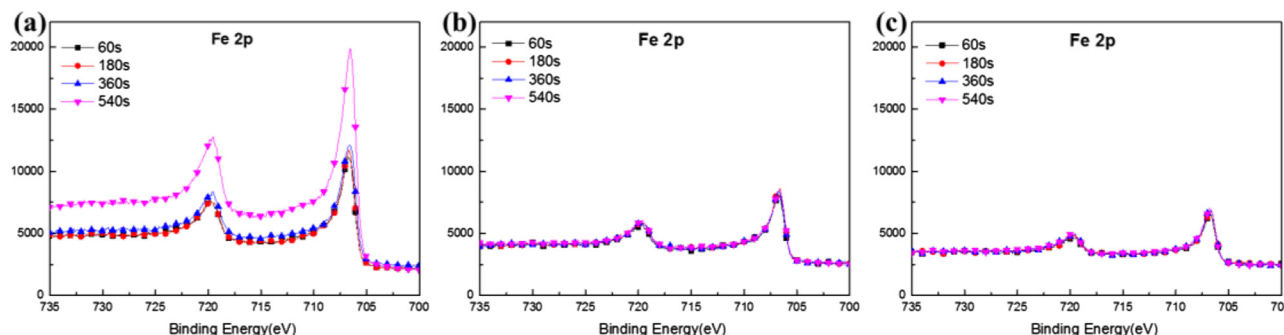

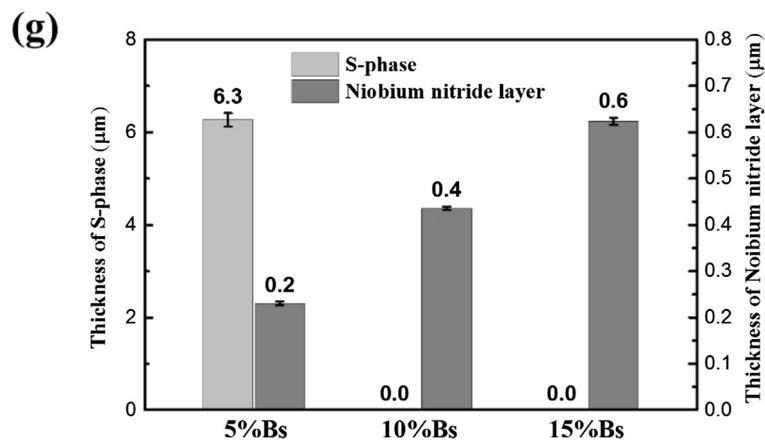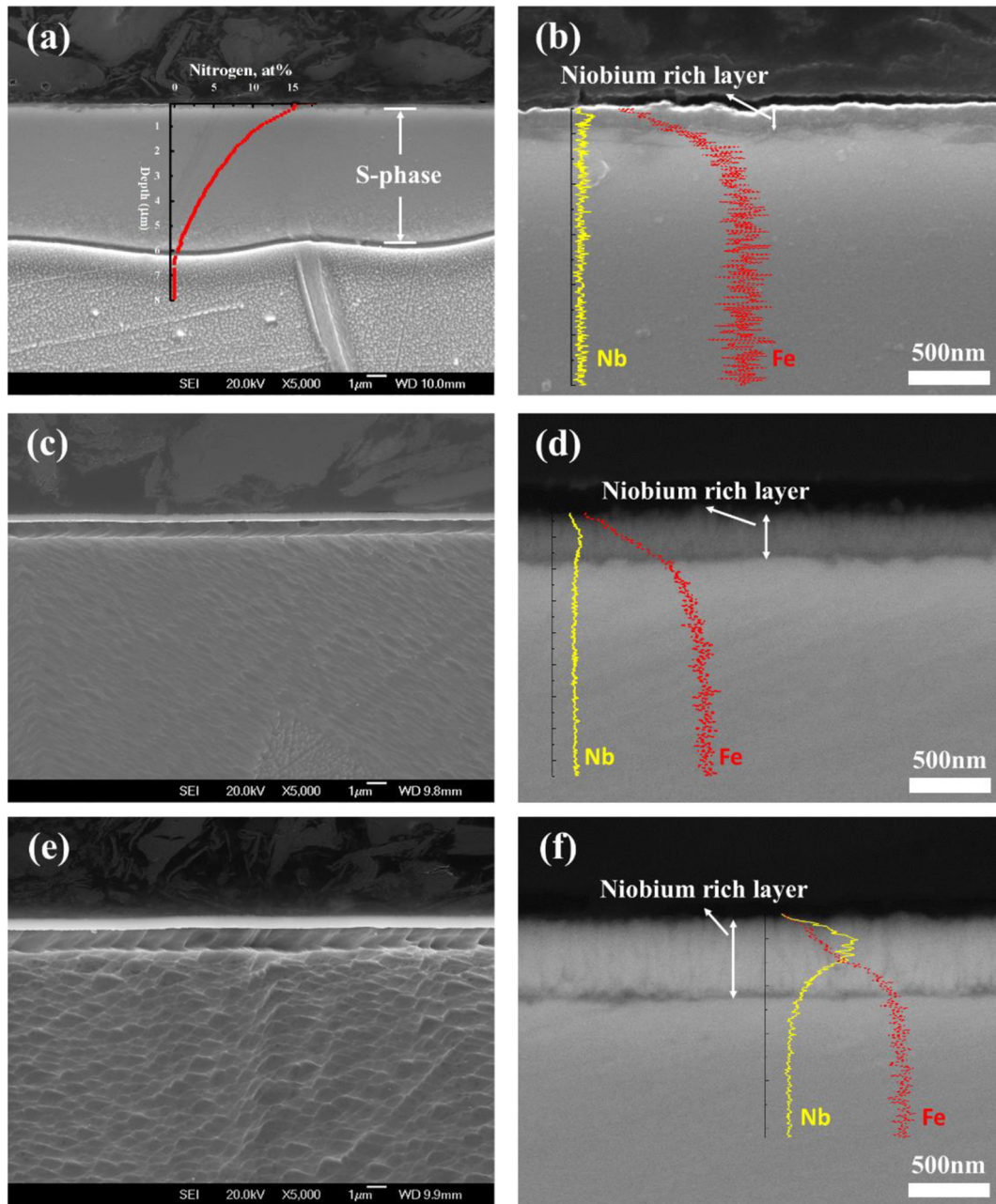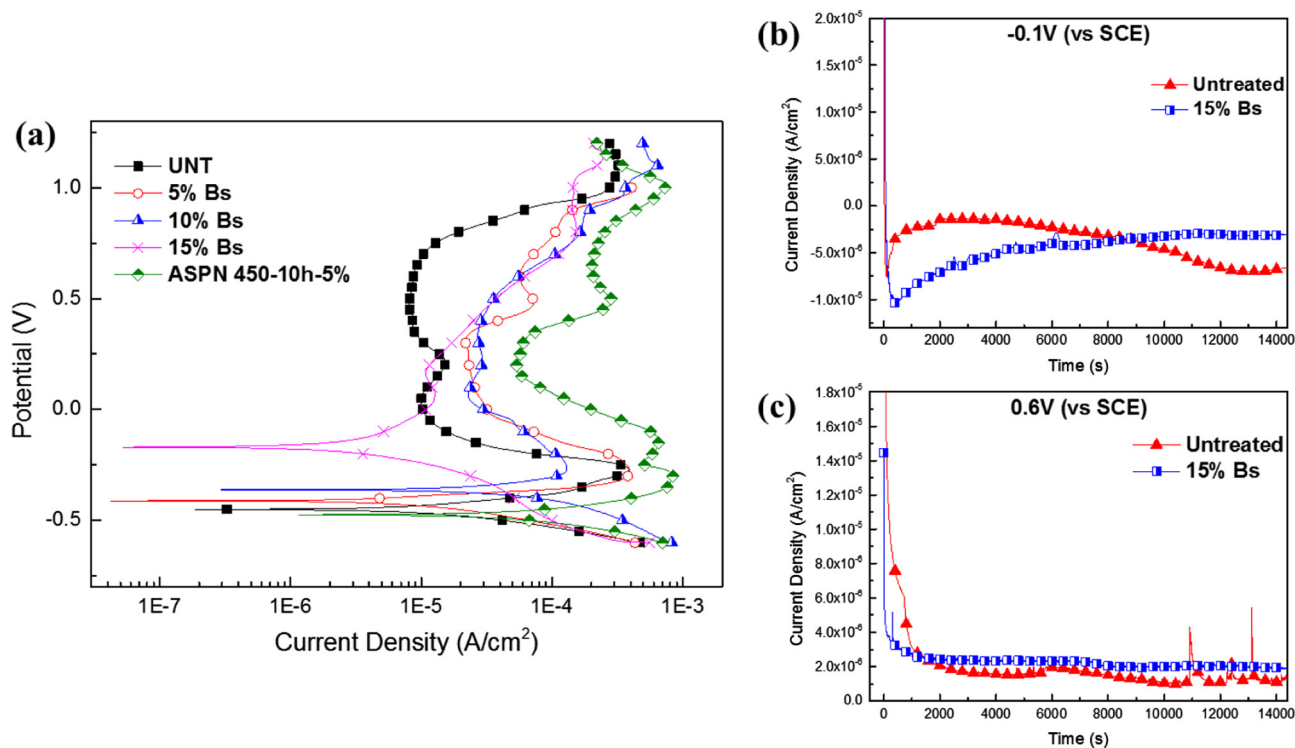Fig. 5 – The Fe 2p XPS spectrums of ASPA(N + Nb) samples (a) 5%Bs (b) 10%Bs (c) 15%Bs.

Fig. 6 — Cross-sectional images of ASPA(N + Nb) samples: Low magnification image of (a) 5%Bs, (c) 10%Bs, (e) 15%Bs. High magnification image of (b) 5%Bs, (d) 10%Bs, (f) 15%Bs, (g) the thickness of S-phase and deposition layer of ASPA(N + Nb) samples.

Fig. 7 — (a) Potentiodynamic polarization curves of ASPA(N + Nb) samples, and potentiostatic polarization results of the untreated sample and the 15%Bs sample under (b) −0.1 V and (c) 0.6 V.

In particular, the 15%Bs sample showed the lowest passive current density among plasma treated samples, almost one order of magnitude lower than that of the ASPN treated sample.

The corrosion potential (E_{corr}) and corrosion current density (I_{corr}) of all the samples were quantitatively calculated from the potentiodynamic polarization curves and the results are summarized in Table 2. It can be seen that the E_{corr} of the ASPA(N + Nb) treated sample increased with the applied bias and was much higher than that of the untreated and the ASPN treated sample. For the corrosion current density, the 10%Bs sample showed a higher I_{corr} than that of both the 5% Bs and the 15%Bs samples. Two possible reasons might have caused the relatively high corrosion current density of the 10%Bs sample. Firstly, compared with the 15%Bs sample, the niobium nitride layer formed on the 10%Bs sample was too porous (Fig. 2(b)) and too thin (Fig. 6(d)) to protect against the aggressive corrosion solution. Secondly, compared with the 5%Bs sample, no corrosion resistant S-phase case formed in the 10%Bs sample. Hence, severe corrosion would occur when the corrosion solution was penetrated through the pinholes in the niobium nitride layer and reached the substrate. It is obvious from Table 2 that the 15%Bs sample exhibited the best corrosion resistance in terms of the highest corrosion potential and the lowest corrosion current density.

Due to the best potentiodynamic performance, the 15%Bs sample was selected for further potentiostatic polarization tests. The potentiostatic polarization results of the untreated sample and the 15%Bs sample under the applied potential of −0.1 V and 0.6 V are plotted in Fig. 7(b) and (c), respectively. When −0.1 V (vs SCE) was applied (Fig. 7(b)), the current density of the 15%Bs sample gradually increased during the entire test; however, the current density of the untreated sample increased in the first 2000s and then decreased in the rest of the test. Accordingly, the current density of the 15%Bs sample was lower than that of the untreated sample within the first 8500s, and then became larger in the rest of the test. When 0.6 V (vs SCE) was applied (Fig. 7(c)), the 15%Bs sample stabilized more quickly than the untreated sample. However, after stabilization the current density of the 15%Bs sample (2.21×10^{-6} A/cm^2) was slightly higher than that of the untreated sample (1.63×10^{-6} A/cm^2). It is worth to notice that after 11,000s, the current density of the untreated sample fluctuated strongly, which indicated the failure of passive protect film. In contrast, the current density of the 15%Bs sample was stable in the entire test, which indicated the better long-term stability of the niobium nitride layer.

Table 2 — Corrosion potential and corrosion current density of samples.		
Sample	E_{corr} vs SCE (mV)	I_{corr} (μA/cm^2)
Untreated	−450	10.3
5%Bs	−412	9.0
10%Bs	−362	20.8
15%Bs	−170	3.2
ASPN 450-10h-5%	−476	74.8

Surface electrical conductivity

The results of ICR measurements under the compaction force of 140 N/cm^2 are shown in Fig. 8. In echo of the results reported before [19], ASPN treatment can significantly decrease the ICR value of 316 SS. Compared with the ASPN treated sample, the ICR value of 316 SS was further reduced to below the DOE target (10 mΩ cm^2) by simultaneously introducing N and Nb (i.e. ASPA(N + Nb)).

Discussion

The optimal parameters of ASPA(N + Nb) treatment for the application of PEMFC bipolar plates

Two of the most important properties required for high-efficient and long-life bipolar plates are their corrosion resistance and surface electrical conductivity.

It can be seen from Table 2 that the corrosion potential increased with the bias applied and the 15%Bs sample exhibited the highest corrosion potential among all the ASPA(N + Nb) treated samples. Indeed, the corrosion potential of the 15%Bs sample was even higher than that of the untreated material. The results of interfacial contact resistance (ICR) measurement revealed that the ICR values of all the ASPA(N + Nb) samples were around 9 mΩ cm^2 and their difference was within the range of the experimental error.

Therefore, it follows that the 15%Bs sample exhibited the best combination of corrosion resistance and surface conductivity among all three ASPA(N + Nb) samples and hence the optimal parameters of the ASPA(N + Nb) treatment for the application of PEMFC bipolar plates are at 450 °C for 10 h with a bias of 15%.

However, due to the S-phase formed in the 5%Bs sample (Fig. 6(a)), it is expected that the 5%Bs sample should have a higher load bearing capacity than the 15%Bs sample containing no S-phase case (Fig. 6(f)). Therefore, the 5% bias could be the best treatment if the forming of the PEMFC bipolar plates, such as stamping, needs to be carried out after the surface treatment.
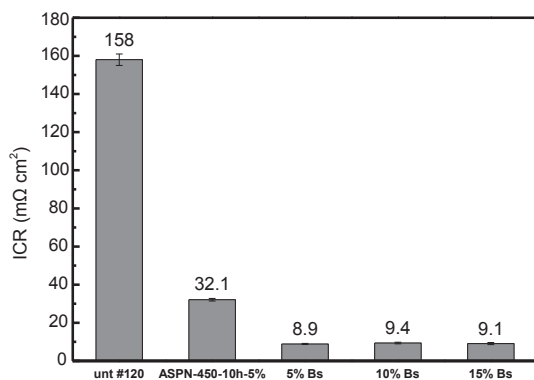
Fig. 8 – The ICR values (under 140 N/cm^2) of ASPA(N + Nb) treated samples as well as untreated and ASPN treated samples for comparison.

Comparison between the ASPN sample and the ASPA(N + Nb) sample

The experimental results reported have clearly demonstrated that the new hybrid plasma surface engineering process developed based on active-screen plasma co-alloying with both interstitial element of nitrogen and substitutional element of niobium was superior to typical active-screen plasma alloying with nitrogen or active screen plasma nitriding (ASPN) treatment in terms of significantly improved corrosion behaviour and effectively reduced ICR to below 10 mΩ cm^2. Therefore, it is scientifically interesting and technologically important to understand the mechanism involved.

To this end, by way of example the ASPN and the ASPA(N + Nb) samples treated under the same processing conditions (at 450 °C for 10 h under 0.75 mbar at 5% bias) are compared in Fig. 9. It can be clearly seen that the thickness of the S-phase case (Fig. 9(a)) formed on the ASPN treated sample (10.8 μm) was much thicker than that formed on the ASPA(N + Nb) treated sample (6.3 μm). Not only is the S-phase thickness different for those two samples, but the nitrogen depth profiles (Fig. 9(b)) also show a great difference. As shown in Fig. 9(b), the nitrogen depth profile across the ASPN treated sample was well above that of the ASPA(N + Nb) sample and the former penetrated much deeper than the latter. This could explain the smaller angle shifting of the S-phase peaks in the XRD profile of the 5%Bs ASPA(N + Nb) sample (Fig. 3) than that of the ASPN treated sample.

The comparison of nano-hardness depth profiles of the ASPN treated sample and the ASPA(N + Nb) treated sample is showed in Fig. 9(c). The hardness of the S-phase case formed in the ASPN treated sample was about 14 GPa and the high hardness region extended to a depth around 10 μm. In contrast, the hardness of S-phase formed in the ASPA(N + Nb) treated sample reduced continuously from around 10 GPa at the surface to the substrate value at about 6 μm below the surface. The observed hardness depth distribution in the ASPN and ASPA(N + Nb) treated samples corresponded well with the nitrogen depth distribution, shown in Fig. 9(b).

Clearly, more nitrogen was introduced into the ASPN treated sample than into the ASPA(N + Nb) treated sample when treated under the same temperature, time, pressure and bias conditions. The major difference in nitrogen mass transfer should be attributed to the Nb introduced during the ASPA(N + Nb) treatments in which a Nb-containing active-screen lid was used. It is known that niobium has a high affinity with nitrogen as it is a strong nitride former [33]. Therefore it is reasonable to assume that most of the nitrogen atoms would react with niobium to form niobium nitride during the ASPA(N + Nb) treatments and hence only a small amount of nitrogen atoms could diffuse into the substrate to form S-phase due to the trapping effect of niobium. Accordingly, the thickness of the S-phase case formed in the ASPA(N + Nb) treated sample was only half that formed in the ASPN sample and the nitrogen content of the former was much lower than that of the latter. This is supported by surface layer structure observed for 10%Bs and 15%Bs samples.

As shown in Fig. 6(d) and (f), further increase in the bias led to the formation of a relatively thick niobium nitride layer on the top of the 10%Bs and 15%Bs samples without measurable S-phase case beneath (Fig. 6(g)). This is because, when increased the bias, Nb was more rapidly sputtered off from the Nb-containing active-screen lid and reacted with nitrogen atoms to form niobium nitride, which deposited onto the sample surface to become a niobium nitride barrier layer for nitrogen diffusion into the subsurface. The formation of Nb_4N_5 layer was implied by the XRD results shown in Fig. 3 and evidenced by the quantitative XPS results (Fig. 4(g)) that the Nb/N ratio (0.87 and 0.81 for 10%Bs and 15%Bs samples respectively) was close to the theoretical value of Nb_4N_5 phase (0.80).

In contrast, although the XPS results shown in Fig. 4(a) and (b) confirmed the formation of niobium nitride during the 5%Bs treatment, it is most probably that no continues niobium nitride film was formed on the top of the 5%Bs sample. This is supported by the XPS quantitative composition results (Fig. 4(g)) because the ratio of Nb/N in the 5%Bs surface (0.54) was much lower than the theoretical Nb/N in the XRD detected Nb_4N_5 phase (0.80). Therefore, nitrogen could still diffuse, despite of trapping by niobium, inward to form a sublayer of S-phase beneath the top Nb-rich layer.

Thus it follows from the discussion above that the new hybrid plasma process developed could produce an in-site formed duplex surface structure consisting of a Nb-rich surface layer followed by a nitrogen supersaturated S-phase case if a low bias of 5% is applied.

The significant improvement in the surface electrical conductivity of 316 SS by the new ASPA(N + Nb) treatments could be contributed to the change of the nature of surface layers. As discussed in introduction, the formation of a passive oxide layer leads to the 'stainlessness' of 316 SS; however it also dramatically increases the electrical resistance from 77 $\mu\Omega$ cm for 316 SS [34] to around 10^8 $\mu\Omega$ cm for the surface chromium oxide (Cr_2O_3) passivation film [35]. In contrast, the surface of the ASPA(N + Nb) treated samples was covered by a niobium nitride layer. The electrical resistance [36] of the surface niobium nitride layer (57 $\mu\Omega$ cm) is 7 orders of magnitude lower than that of the surface chromium oxide (Cr_2O_3) passivation film. As a result, the ICR value has been significantly reduced from 316 SS (158 mΩ cm^2) to ASPA(N + Nb) treated samples (9 mΩ cm^2). From the comparison of ICR in Fig. 8, the ICR value of the ASPA(N + Nb) treated samples was also much lower than that of the typical ASPN treated samples. This is mainly because chromium oxide can still form on the
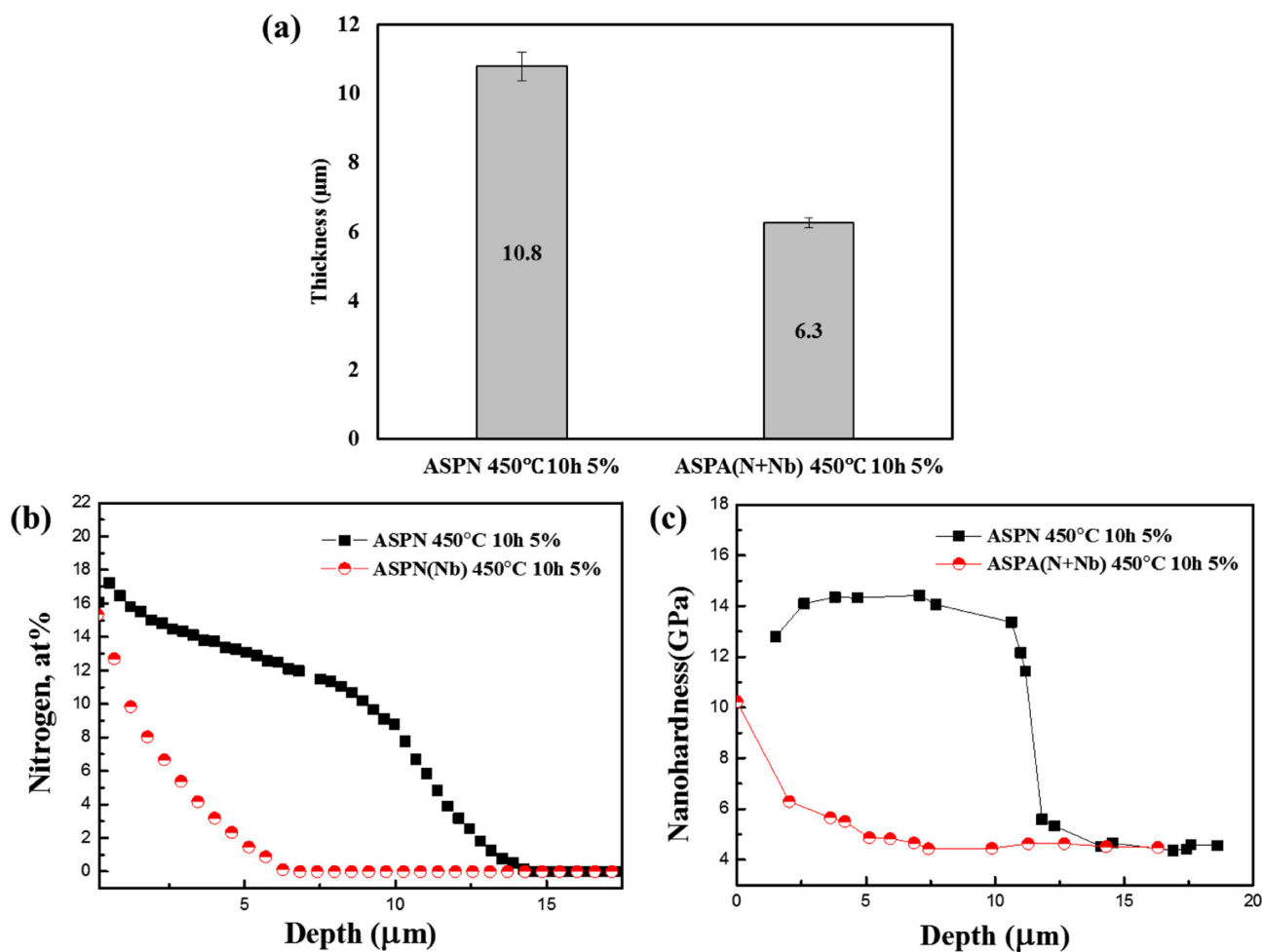

Fig. 9 – (a) the S-phase thickness, (b) atomic percentage of nitrogen profiles against depth and (c) nano-hardness profiles of ASPN and ASPA(N + Nb) samples treated at 450 °C for 10 h with 5% bias.

surface of S-phase formed in austenite stainless steel by the ASPN treatments [37].

Apart from the effectively improved surface electrical conductivity, the corrosion resistance of the ASPA(N + Nb) treated samples was also superior to that of the typical ASPN treated samples in terms of reduced corrosion current density and increased corrosion potential. This could be attributed to the formation of surface niobium nitride layer by the ASPA(N + Nb) treatment in view of the superior corrosion resistance of the niobium nitride [38]. As reported in our previous paper [19], the surface of the ASPN treated 316 SS is covered by a layer of iron nitrides [39], which exhibits poor corrosion behaviour than niobium nitride. The slightly higher passive current density of the ASPA(N + Nb) treated 316 SS relative to that of the untreated material could be related to the corrosion of iron embedded in the niobium nitride layer (Fig. 5).

Conclusions

A new hybrid plasma surface co-alloying process has been successfully developed to simultaneously alloy 316 austenitic stainless steel (316 SS) surfaces with both nitrogen and niobium. By adjusting the treatment condition, the layer structure of the modified surfaces can be tailored. When treated under a low applied bias of 5%, a duplex surface layer structure consisting of a very thin niobium nitride surface layer followed by an S-phase case can be produced; however, when treated under high applied bias (10–15%), only a niobium nitride layer can be formed on the surface without the formation of S-phase case underneath.

The electrochemical corrosion resistance and the interfacial contact resistance (ICR) of the ASPA(N + Nb) treated surfaces have been evaluated and compared with untreated and typical active screen plasma nitrided (ASPN) surfaces. The electrochemical corrosion tests have revealed that the corrosion potential of 316 SS can be increased by all three ASPA(N + Nb) treatments but the passive current density of the treated samples was higher than that of the untreated one; the ASPA(N + Nb) treated samples were superior to the ASPN treated ones in terms of increased corrosion potential and reduced passive current density. Among the three ASPA(N + Nb) treated samples, the 15%Bs sample exhibited the best corrosion resistance.

The results of interfacial contact resistance tests show that the ICR values of all three ASPA(N + Nb) treated samples were about 9 mΩ cm^2. This is about 18 and 3.6 times lower than that of the untreated and ASPN treated 316 SS, respectively, which is also lower than the DOE target (10 mΩ cm^2).

Taking the corrosion properties and interfacial contact resistant into account, the ASPA(N + Nb) treatment at 15% bias (15%Bs) is the best treatment potentially for the application of PEMFC bipolar plates.

Further tests, such as single cell tests and long-duration corrosion tests, are needed to evaluate the performance of the ASPA(N + Nb) treated 316 stainless steel bipolar plates in the real PEMFC working environment.

REFERENCES

[1] Steele B, Heinzel A. Materials for fuel-cell technologies. Nature 2001;414:345–52.

[2] Jin CK, Kang CG. Fabrication by vacuum die casting and simulation of aluminum bipolar plates with micro-channels on both sides for proton exchange membrane (PEM) fuel cells. Int J Hydrogen Energy 2012;37:1661–76. http://dx.doi.org/10.1016/j.ijhydene.2011.10.050.

[3] Fetohi AE, Abdel Hameed RM, El-Khatib KM. Ni–P and Ni–Mo–P modified aluminium alloy 6061 as bipolar plate material for proton exchange membrane fuel cells. J Power Sources 2013;240:589–97. http://dx.doi.org/10.1016/j.jpowsour.2013.04.085.

[4] Zhang D, Duan L, Guo L, Wang Z, Zhao J, Tuan W-H, et al. TiN-coated titanium as the bipolar plate for PEMFC by multi-arc ion plating. Int J Hydrogen Energy 2011;36:9155–61. http://dx.doi.org/10.1016/j.ijhydene.2011.04.123.

[5] Ren Z, Zhang D, Wang Z. Stacks with TiN/titanium as the bipolar plate for PEMFCs. Energy 2012;48:577–81. http://dx.doi.org/10.1016/j.energy.2012.10.020.

[6] Yokoyama M, Yamaura S, Kimura H, Inoue A. Production of metallic glassy bipolar plates for PEM fuel cells by hot pressing in the supercooled liquid state. Int J Hydrogen Energy 2008;33:5678–85. http://dx.doi.org/10.1016/j.ijhydene.2008.07.034.

[7] Kim S, Yamaura S, Makino A, Inoue A. Production of Ni-P amorphous alloy-coated bipolar plate for PEM fuel cell by electro-less plating. Mater Trans 2011;52:709–13. http://dx.doi.org/10.2320/matertrans.MBW201007.

[8] Antunes RA, Oliveira MCL, Ett G, Ett V. Corrosion of metal bipolar plates for PEM fuel cells: a review. Int J Hydrogen Energy 2010;35:3632–47. http://dx.doi.org/10.1016/j.ijhydene.2010.01.059.

[9] Tawfik H, Hung Y, Mahajan D. Metal bipolar plates for PEM fuel cell—a review. J Power Sources 2007;163:755–67. http://dx.doi.org/10.1016/j.jpowsour.2006.09.088.

[10] Karimi S, Fraser N, Roberts B, Foulkes FR. A review of metallic bipolar plates for proton exchange membrane fuel cells: materials and fabrication methods. Adv Mater Sci Eng 2012:2012. http://dx.doi.org/10.1155/2012/828070.

[11] André J, Antoni L, Petit J-P. Corrosion resistance of stainless steel bipolar plates in a PEFC environment: a comprehensive study. Int J Hydrogen Energy 2010;35:3684–97. http://dx.doi.org/10.1016/j.ijhydene.2010.01.062.

[12] Feng K, Wu G, Li Z, Cai X, Chu PK. Corrosion behavior of SS316L in simulated and accelerated PEMFC environments. Int J Hydrogen Energy 2011;36:13032–42. http://dx.doi.org/10.1016/j.ijhydene.2011.07.058.

[13] Davies D, Adcock P, Turpin M, Rowen S. Stainless steel as a bipolar plate material for solid polymer fuel cells. J Power Sources 2000;86:237–42. http://dx.doi.org/10.1016/S0378-7753(99)00524-8.

[14] Yang Y, Ning X, Tang H, Guo L, Liu H. Effects of passive films on corrosion resistance of uncoated SS316L bipolar plates for

proton exchange membrane fuel cell application. Appl Surf Sci 2014. http://dx.doi.org/10.1016/j.apsusc.2014.09.049.

[15] Hermann A, Chaudhuri T, Spagnol P. Bipolar plates for PEM fuel cells: a review. Int J Hydrogen Energy 2005;30:1297–302. http://dx.doi.org/10.1016/j.ijhydene.2005.04.016.

[16] Tian R, Sun J. Corrosion resistance and interfacial contact resistance of TiN coated 316L bipolar plates for proton exchange membrane fuel cell. Int J Hydrogen Energy 2011;36:6788–94. http://dx.doi.org/10.1016/j.ijhydene.2011.03.021.

[17] Yun Y-H. Deposition of gold–titanium and gold–nickel coatings on electropolished 316L stainless steel bipolar plates for proton exchange membrane fuel cells. Int J Hydrogen Energy 2010;35:1713–8. http://dx.doi.org/10.1016/j.ijhydene.2009.12.036.

[18] Husby H, Kongstein OE, Oedegaard A, Seland F. Carbon-polymer composite coatings for PEM fuel cell bipolar plates. Int J Hydrogen Energy 2014;39:951–7. http://dx.doi.org/10.1016/j.ijhydene.2013.10.115.

[19] Lin K, Li X, Sun Y, Luo X, Dong H. Active screen plasma nitriding of 316 stainless steel for the application of bipolar plates in proton exchange membrane fuel cells. Int J Hydrogen Energy 2014;39:21470–9. http://dx.doi.org/10.1016/j.ijhydene.2014.04.102.

[20] Papageorgopoulos D. DOE fuel cell technology program overview and introduction to the 2010 fuel cell pre-solicitation workshop in DOE fuel cell pre-solicitation workshop. Lakewood, Color: Dep Energy; 2010.

[21] Weil K, Xia G, Yang Z, Yongkim J. Development of a niobium clad PEM fuel cell bipolar plate material. Int J Hydrogen Energy 2007;32:3724–33. http://dx.doi.org/10.1016/j.ijhydene.2006.08.041.

[22] Pozio A, Silva R, Masci A. Corrosion study of SS430/Nb as bipolar plate materials for PEMFCs. Int J Hydrogen Energy 2008;33:5697–702. http://dx.doi.org/10.1016/j.ijhydene.2008.05.099.

[23] Kim J, Kim S, You Y, Kim D, Hong S, Suh H, et al. Niobium sputter coated stainless steel as a bipolar plate material for polymer electrolyte membrane fuel cell stacks. Int J Electrochem Sci 2011;6:4365–77.

[24] Kim J-H, Jung D-W, Kim S, Hong S, You Y, Kim D. Durability of a niobium thin film for bipolar plates in PEMFC. Vacuum 2012;86:1789–94. http://dx.doi.org/10.1016/j.vacuum.2012.03.042.

[25] Cao C, Liang C, Huang N. Electrochemical behavior of stainless steel with niobium electrodeposited in [emim] OTf ionic liquids in PEMFC environment. Rare Met Mater Eng 2013;42:569.

[26] Hong S-T, Weil KS. Niobium-clad 304L stainless steel PEMFC bipolar plate material. J Power Sources 2007;168:408–17. http://dx.doi.org/10.1016/j.jpowsour.2007.03.032.

[27] Feng K, Li Z, Cai X, Chu PK. Corrosion behavior and electrical conductivity of niobium implanted 316L stainless steel used as bipolar plates in polymer electrolyte membrane fuel cells. Surf Coatings Technol 2010;205:85–91. http://dx.doi.org/10.1016/j.surfcoat.2010.06.009.

[28] Wang H. Stainless steel as bipolar plate material for polymer electrolyte membrane fuel cells. J Power Sources 2003;115:243–51. http://dx.doi.org/10.1016/S0378-7753(03)00023-5.

[29] Dong H. S-phase surface engineering of Fe-Cr, Co-Cr and Ni-Cr alloys. Int Mater Rev 2010;55:65–98. http://dx.doi.org/10.1179/095066009X12572530170589.

[30] Olaya JJ, Huerta L, Rodil SE, Escamilla R. Superconducting niobium nitride films deposited by unbalanced magnetron sputtering. Thin Solid Films 2008;516:8768–73. http://dx.doi.org/10.1016/j.tsf.2008.06.065.

[31] Jack KH. The occurrence and the crystal structure of formula-iron nitride; a new type of interstitial alloy formed during the tempering of nitrogen-martensite. Proc R Soc A Math Phys Eng Sci 1951;208:216–24. http://dx.doi.org/10.1098/rspa.1951.0155.

[32] Li XY, Dong H. Effect of annealing on corrosion behaviour of nitrogen S phase in austenitic stainless steel. Mater Sci Technol 2003;19:1427–34. http://dx.doi.org/10.1179/026708303225007924.

[33] Brauer G. Nitrides, carbonitrides and oxynitrides of niobium. J Less Common Met 1960;2:131–7.

[34] Ho CY, Chu TK. Electrical resistivity and thermal conductivity of nine selected AISI stainless steels. DTIC Doc 1977.

[35] Cheng C-S, Gomi H, Sakata H. Electrical and optical properties of Cr203 films prepared by chemical vapour deposition. Phys Status Solidi 1996;417:417–25.

[36] Nigro A, Nobile G, Rubino MG, Vaglio R. Electrical resistivity of polycrystalline niobium nitride films. Phys Rev B 1988;37:3970–2. http://dx.doi.org/10.1103/PhysRevB.37.3970.

[37] Nikolov K, Köster K, Kaestner P, Bräuer G, Klages CP. Strip hollow cathode method for plasma thermochemical treatment for surface modification of thin metal strips: plasma nitriding of austenitic stainless steel sheets for bipolar plates. Vacuum 2014;102:31–7. http://dx.doi.org/10.1016/j.vacuum.2013.11.001.

[38] Wang L, Sun J, Sun J, Lv Y, Li S, Ji S, et al. Niobium nitride modified AISI 304 stainless steel bipolar plate for proton exchange membrane fuel cell. J Power Sources 2012;199:195–200. http://dx.doi.org/10.1016/j.jpowsour.2011.10.034.

[39] Corujeira Gallo S, Dong H. On the fundamental mechanisms of active screen plasma nitriding. Vacuum 2009;84:321–5. http://dx.doi.org/10.1016/j.vacuum.2009.07.002.